PAPER

High-temperature colossal dielectric behavior of BaZrO$_3$ ceramics

Lei Tong, [ID] Haibo Li, Wei Ni, Youmin Guo,* Qiuju Li, Hong Wang and Chunchang Wang*

BaZrO$_3$ (BZO) powders were synthesized by solution combustion based on the glycine nitrate process. The sintering conditions of the BZO sample were optimized by varying the sintering temperature and dwell time. The dielectric properties of the sintered samples were investigated in the temperature range of 300–1080 K and frequency range of 10^2 to 10^6 Hz. The sample sintered at 1973 K for 12 h was found to show the best dielectric properties. Detailed investigations on this sample reveal an incipient ferroelectric behavior in the temperature range below 420 K and a colossal dielectric behavior above 420 K. The colossal dielectric behavior is composed of two thermally activated relaxations. The low-temperature relaxation was argued to be a dipolar relaxation caused by an oxygen vacancy hopping motion inside grains and the high-temperature one was ascribed to a Maxwell–Wagner relaxation due to the oxygen vacancies being blocked by the sample/electrode contacts.

1. Introduction

Materials showing colossal dielectric constants (CDCs, dielectric constants larger than 10^3) have drawn considerable attention due to their promising potential for application in the area of device miniaturization and energy storage.[1–3] There are currently two main types of CDC material systems. The traditional type of CDC material is ferroelectric perovskites, which show dielectric constants up to 10^4 to 10^5 around the ferroelectric phase transition,[4] but suffer from strong temperature dependence. Another type of CDC material system is the plethora of non-ferroelectric oxides represented by CaCu$_3$Ti$_4$O$_{12}$.[5–7] The CDC behavior of this type of material is characterized by a colossal and temperature stable dielectric constant plateau around room temperature. This dielectric plateau decreases in a step-like manner to a low dielectric constant plateau at low enough temperature. Meanwhile a relaxation peak appears in the corresponding dielectric loss. The high-temperature dielectric plateau is promising for practical applications. Nevertheless, the remarkable dielectric loss in this temperature range limits its application. The low-temperature dielectric plateau, on the contrary, is independent of both frequency and temperature with very low dielectric loss. This feature is very desirable for device applications. But for most CDC materials, the low-temperature plateau appears at temperatures far below room temperature (RM). For example, the plateau appears below 100, 120, and 200 K for Ba$_2$CoNbO$_6$,[8]

Na$_{0.5}$Bi$_{0.5}$Cu$_3$Ti$_4$O$_{12}$,[9] and TbFeO$_3$ (ref. 10) recorded at 10 kHz, respectively. In order to circumvent this limitation, the search for materials exhibiting such kind of dielectric plateau at or above RM is of vital importance. Recently, our group has reported that CaLaAlO$_4$ ceramics showed CDC behavior in the temperature above RM.[11] The typical feature of this material is that it contains no transition metal ions and the CDC behavior is caused by the electromigration of oxygen vacancies. This work provides a heuristic hint to search for high-temperature CDC materials in oxides free of transition metal ions.

Proton conductors based on cerate and zirconate perovskite oxides have attracted considerable attention in recent years for electrochemical applications, such as fuel cells, separation membranes, and steam electrolysers.[12,13] Of the known perovskite-type proton conductors, there has been considerable experimental interest in acceptor-doped BaZrO$_3$ (BZO) due to its high proton conductivity in a cubic structure coupled with good chemical and mechanical stability.[14,15] The electric properties of pure BZO, however, is dominated by oxygen vacancies.[16,17] On the other hand, the Zr^{4+} is very stable (with respect to Ti^{4+}). This fact makes BZO similar to a material free of transition metal ions. Therefore, high-temperature CDC behavior could be expected in BZO. However, to the best of our knowledge, dielectric properties of BZO were performed in low-temperature range below RM[18] or on Ti-doped samples.[19–21] There are no reports on the dielectric properties of BZO above RM.

In this paper, we performed investigations on high-temperature (300 to 1080 K) dielectric properties of BZO ceramics. As expected, the sample showed high-temperature CDC behavior composed of two relaxations. The mechanisms of these relaxations were discussed.

Laboratory of Dielectric Functional Materials, School of Physics & Material Science, Anhui University, Hefei 230601, China. E-mail: youminguo@ahu.edu.cn; ccwang@ahu.edu.cn

2. Experimental details

BZO samples were synthesized by solution combustion based on the glycine nitrate process. Stoichiometric amounts of barium nitrate $(Ba(NO_3)_2)$ (0.04 mol) and zirconium nitrate $(Zr(NO_3)_4 \cdot 5H_2O)$ (0.04 mol) were dissolved in deionized water (800 mL) to form a solution. Glycine was then added at a molar ratio of glycine (0.16 mol) to total metallic cations of 2. The water in the solution was evaporated by heating over a hot plate while stirring until a gel was formed. The gel was moved to an electric oven at 513 K triggering auto-combustion. The resulting primary powders were further calcined at 1373 K for 5 h in ambient air. After cooling to room temperature naturally, pellets of 11 mm diameter and approximately 1 mm thickness were pressed and sintering at different conditions. The phase purity of the synthesized powders was characterized by X-ray diffraction (XRD) on a Rigaku SmartLab diffractometer (Rigaku Beijing Co., Beijing, China) with Cu Kα radiation. The microstructure and grain size of the sintered pellets were studied using a field-emission scanning electric microscope (SEM, Model S-4800, Hitachi Co., Tokyo, Japan). The temperature-dependent dielectric properties were measured using a Wayne Kerr 6500B precise impedance analyzer with the sample mounted in a holder placed inside a PST-2000HL dielectric measuring system (Partulab Co., Wuhan, China). The temperature variations were automatically controlled using a PCT10 Stanford temperature controller with a heating rate of 3 K min^{-1}. The ac measuring signal was 100 mV. Annealing treatments were performed in oxygen and nitrogen (both with purity > 99.999%) at 1073 K for 2 h with flow rate of 200 mL min^{-1}.

3. Results and discussion

Fig. 1 shows the room-temperature XRD pattern of synthesized BZO powders in the 2θ range of 20 to 80°. The pattern can be indexed based on a cubic structure with $Pm\bar{3}m$ space group (JCPDS file no. 06-0399), and no impurity phases were observed. In order to obtain a BZO sample with high relative density for

dielectric measurements, the pressed BZO pellets were sintered at different conditions.

Fig. 2 presents the SEM images of the sintered BZO ceramics. It can be seen that all samples present distinct grain structure. The average grain size and relative density are summarized in Table 1. From which, it is clearly seen that both the grain size and relative density increase with increasing sintering temperature and dwell time. The sample sintered at 1973 K for 12 h was found to show the highest relative density with a value of 98.1%.

Fig. 3 compares the temperature dependence of dielectric constant, ε' (the real part of the complex permittivity ε^*) and dielectric loss tangent $\tan \delta(T)$ ($\tan \delta = \varepsilon''/\varepsilon'$, ε'' is the imaginary part of complex permittivity) for BZO ceramics prepared at different sintering conditions. It is seen that no CDC behavior can be found in the sample sintered at 1773 K for 12 h. When the sintering temperature is elevated to 1873 K, the $\varepsilon'(T)$ curve steplike increases from a low-temperature plateau around 27.5 to a high-temperature plateau with values over 300. Meanwhile, the corresponding $\tan \delta(T)$ shows a peak. These features resemble the CDC behavior except for the not high enough value of the high-temperature plateau. As the sintering temperature is elevated higher than 1923 K, the high-
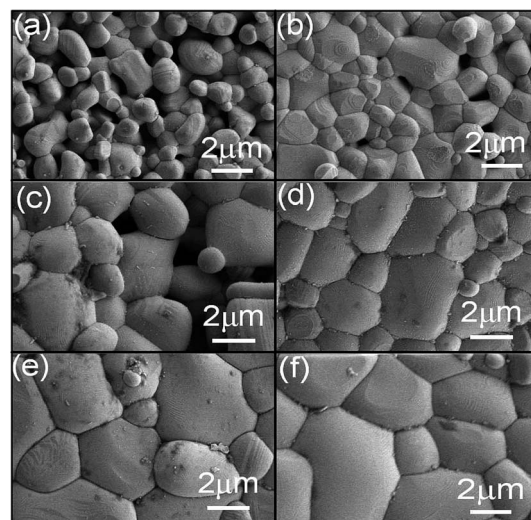

Fig. 2 SEM surface images of the BZO samples prepared at various sintering conditions: (a) 1773 K for 12 h, (b) 1873 K for 12 h, (c) 1923 K for 6 h, (d) 1923 K for 12 h, (e) 1973 K for 6 h, and (f) 1973 K for 12 h.
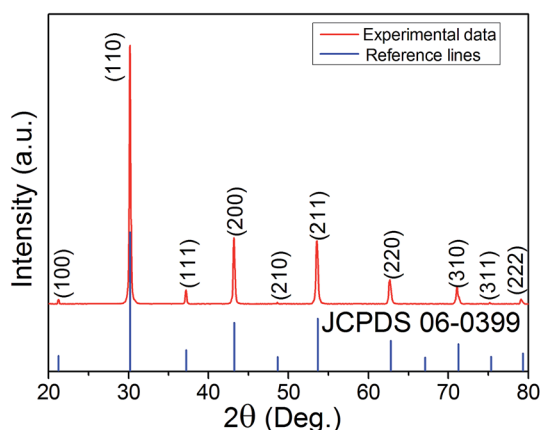
Table 1 The average grain size, standard deviation and relative density of the BZO pellets prepared at different sintering conditions

Sintering condition	Average grain size (μm)	Standard deviation (μm)	Relative density (%)
1773 K–12 h	1.05	0.20	90.8
1873 K–12 h	1.65	0.36	93.0
1923 K–6 h	2.73	0.62	95.2
1923 K–12 h	3.13	0.83	96.3
1973 K–6 h	3.47	0.92	96.3
1973 K–12 h	4.19	0.95	98.1

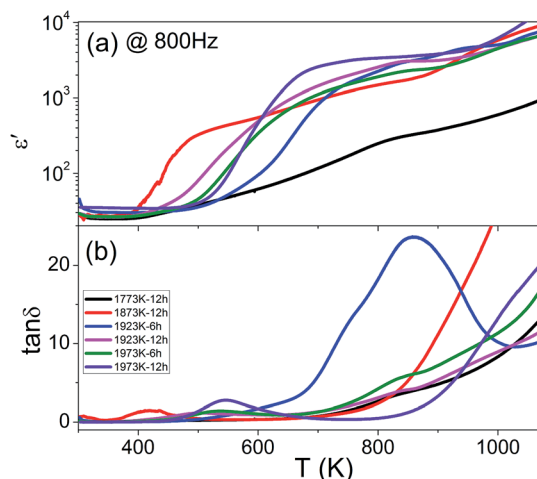**Fig. 1** The XRD pattern of the synthesized BZO powders recorded at room temperature.

Fig. 3 The dielectric permittivity (a) and loss tangent (b) as a function of temperature for BZO ceramics prepared at different sintering conditions. The curves were recorded with a frequency of 800 Hz.

temperature plateau shows values larger than 10^3, indicating that the CDC behavior appears in these samples. To judge the merit of the CDC behavior, quality criteria, such as high dielectric constant, low dielectric loss, and good temperature stability have been put forward. Based on these factors, it is not difficult to find out that the sample sintered at 1973 K for 12 h shows the optimum properties. We, therefore, perform detailed dielectric investigations focusing on this sample in the following part.

Fig. 4 displays the temperature dependence of $\varepsilon'(T)$ and tan $\delta(T)$ measured with various frequencies for BZO sintered at 1973 K for 12 h. In the temperature range below 420 K, both $\varepsilon'(T)$ and tan $\delta(T)$ behave as plateaus independent of frequency and temperature. This can be ascribed to the intrinsic dielectric properties resulting from the electronic and/or ionic polarization. The flat dielectric constant was found to be ~34.8, which
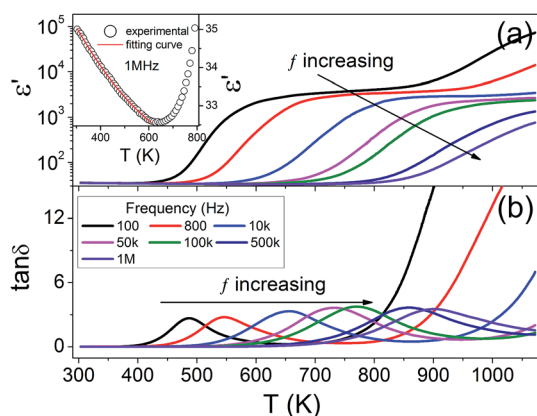

Fig. 4 The temperature dependence of (a) dielectric constant and (b) loss tangent for BZO measured with different frequencies. The inset of (a) is an enlarged view of dielectric constant recorded at 1 MHz in the low temperature range, which compares the experimental data (open circles) and the fitting curve (solid line) based on the Barrett equation [eqn (1)].

agreed well with the previously reported values of 32–37.[21,22] However, a careful examination reveals that the dielectric constant plateau is actually a frequency-independent decline similar to that found in $SrTiO_3$ and $KTaO_3$.[23–25] This behavior is the typical feature for incipient ferroelectrics. To further confirm the incipient ferroelectric nature in the present sample, the data recorded with 1 MHz were fitted using the Barrett equation:[26]

$$\varepsilon'(T) = C\left(\frac{T_1}{2}\coth\left(\frac{T_1}{2T}\right) - T_0\right)^{-1} + B \tag{1}$$

where C is a constant, T_0 is hypothetical Curie temperature, T_1 is onset temperature of quantum fluctuations, and B is dielectric constant at high-frequency limit. The fitting result as well as the experimental data were given in the insert of Fig. 4(a). Perfect agreement between the experimental data and fitting result was achieved. The fitting yields the parameters of $B = 28.54$, $C = 5454$, $T_1 = 309$ K, and $T_0 = -18$ K. These values are comparable with those previously reported in BaZrO$_3$,[20] indicating that the incipient ferroelectric behavior exists in the present sample. With further increasing temperature, the sample exhibits CDC behavior similar to that reported in CaCu$_3$Ti$_4$O$_{12}$.[6] The CDC behavior is found to be composed of two stepwise increases occurring around 500 and 900 K (for the curve recorded under 100 Hz). Meanwhile, two sets of peaks in the curves of the dielectric loss tangent are observed. The positions of both sets of peaks shift to high temperature with increasing frequency. This indicates that there are two thermally activated relaxations in BZO. To discuss each relaxation clearly, the two relaxations were referred to as $R1$ and $R2$ in the order of ascending temperature.

To understand the mechanism of the observed relations, we try to calculate the relaxation parameters for each relaxation. But $R2$ in tan $\delta(T)$ is obscured by the increasing background, which makes it difficult to deduce its position accurately. To overcome this shortcoming, the dielectric function of electric modulus M^* ($=M' + jM'' = 1/\varepsilon^*$, where, $j = \sqrt{-1}$) is applied. It was suggested that electric modulus could provide valuable information about relaxation mechanism in the absence of a well-defined dielectric loss peak in tan $\delta(T)$. Fig. 5 shows the imaginary part of the electric modulus $M''(T)$ as a function of temperature under various frequencies ranging from 100 Hz to 1 MHz for BZO ceramics. Owing to the absence of the increasing background, a set of thermally activated relaxation can be clearly seen. The inset (a) is an enlarged view of the $M''(T)$ curves in the high-temperature range as indicated by the rectangle. It clearly shows the high-temperature relaxation. The electric modulus spectra substantially confirm the two sets of relaxations in BZO. To calculate the relaxation parameters, the measuring frequency (f) and the peak position (T_P) was plotted according to the Arrhenius law:

$$f = f_0 \exp(-E_a/k_B T_P) \tag{2}$$

where f_0 is eigenfrequency, E_a is activation energy for relaxation and k_B is Boltzmann constant. Arrhenius plots for $R1$ and $R2$ (closed points) along with the linear fits (straight lines through
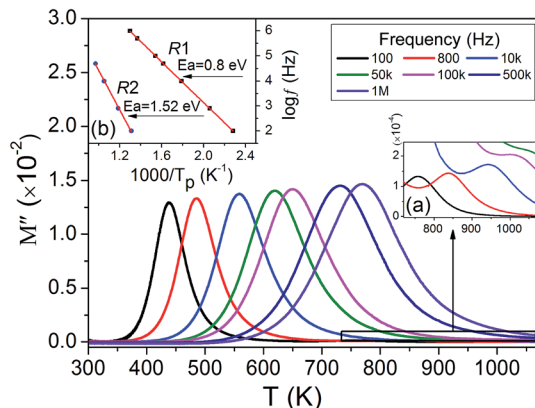
Fig. 5 The imaginary part of electric modulus as a function of temperature for BZO sample at various frequencies. The inset (a) is an enlarged view of the rectangle region as indicated by the arrow. The inset (b) shows the Arrhenius plots of $R1$ and $R2$. The solid lines in the inset are the linear fitting results.

the data points) were shown in the inset (b) of Fig. 5. The relaxation parameters E_a and f_0 was calculated, respectively, to be 0.80 eV and 9.97×10^{10} Hz for $R1$, and 1.52 eV and 1.28×10^{11} Hz for $R2$. The values of the activation energy of both relaxations are comparable with that reported for the thermally activation migration of oxygen vacancies, which has been widely reported to be around 1.0 eV.[27–33] Thus, the observed relaxations might be related to the migration of the oxygen vacancies.

To further clarify this inference, we measured the dielectric properties of BZO after being annealed first in O_2 and then in N_2. Table 2 summaries the values of the relaxation parameters (E_a and f_0) of $R1$ and $R2$ in different cases. From which we can see that the value of activation energy for both relaxations is increased by the O_2-annealing treatment and then decreased by the N_2-annealing treatment. It was reported that the activation energy increases (decreases) with the decreasing (increasing) concentration of oxygen vacancies. Since the concentration of oxygen vacancies can be decreased (increased) by annealing in oxygen (nitrogen),[34] this result firmly confirms that the two relaxations are associated with oxygen vacancies. Our recent results revealed that the hopping motion of oxygen vacancies first created a reorientational dipolar relaxation and then a Maxwell–Wagner relaxation when the vacancies were blocked by interfaces such as grain boundaries.[35] The $R1$ can be reasonably ascribed to be the dipolar relaxation related to the hopping oxygen vacancies, while $R2$ might be the Maxwell–Wagner relaxation related to the blocked oxygen vacancies.

In order to evidence this point, we conduct impedance analysis, as it is a powerful technique to separate the dielectric contributions from bulk (grain), grain boundary and contact effects. Fig. 6(a) and (b) displays the Nyquist plots (Z'' vs. Z', where Z' and Z'' are the real and imaginary parts of the complex impedance Z^*) of BZO sample measured at the temperatures of 450 and 730 K under different DC biases. The complex impedance spectra at 450 K behave as a semicircular arc independent of DC bias confirming bulk dielectric response. At 730 K, the impedance spectra can be separated into two distinct regions: the high-frequency region independent of the DC bias indicative of the bulk response, and the low-frequency region which can be enhanced by increasing the bias. This fact substantially convinces that the low-frequency arc corresponds to interfacial response. However, the interfacial response is usually associated with Schottky barrier that should be depressed rather than enhanced by the DC bias.[36] Our recently report in $ZnNb_2O_6$ ceramics indicated that this abnormal bias behavior was caused by sample/electrodes contacts instead of grain boundaries.[37] This is because that the electrode is electronic conductor instead of ion conductor. When the vacancies are blocked by the interface at the electrode, they can never overcome this barrier. Thus, the DC bias notably enhances the space charge, which, in turn, enhances the Maxwell–Wagner relaxation. This finding strongly supports that $R2$ is related to the blocked oxygen vacancies. The absence of grain boundary effect might be that fact that the BZO shows the largest grain size and its density is very close to that of single crystal [see Table 1]. This implies that the fraction of grain-boundary in BZO is very small. Thus, the influence of grain-boundary is almost negligible.

The above results indicate that $R1$ and $R2$ are related to bulk and interfacial effects, respectively. To further convince this point, we conduct AC conductivity analysis. Fig. 7(a) shows the AC conductivity ($\sigma(\omega)$) as a function of frequency recorded at different temperatures. We note that the curves, especially for those measured at intermediate temperatures, behave as low- and high-frequency plateaus with sigmoidal curves collecting them. The plot can be clarified into two regions (I and II) separated by a dashed line. Obviously, the well-known universal dielectric response (UDR) model fails to describe this kind of AC conductivity behavior,[38] because the UDR conductivity is characterized by the feature of a low-frequency plateau (DC conductivity) followed by a rapid increase in the high-frequency range. To explain this behavior, we presented an equivalent circuit as illustrated in the inset of Fig. 7(a). It contains two

Table 2 Relaxation parameters of $R1$ and $R2$ for BZO samples treated in different annealing conditions

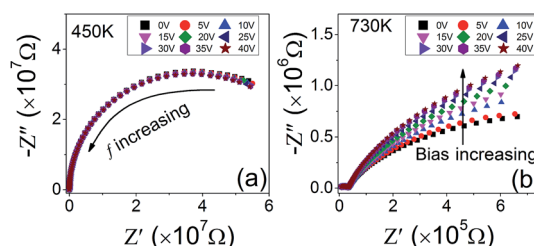| Annealing case	$R1$		$R2$	
	E_a (eV)	f_0 (Hz)	E_a (eV)	f_0 (Hz)
As-prepared	0.80	9.97×10^{10}	1.52	1.28×10^{11}
O_2-annealed	0.94	1.2×10^{12}	1.83	6.31×10^{13}
N_2-annealed	0.74	1.47×10^{11}	1.33	1.08×10^{11}

Fig. 6 Complex impedance of BZO sample at the measured temperatures of (a) 450 and (b) 730 K under various DC biases.
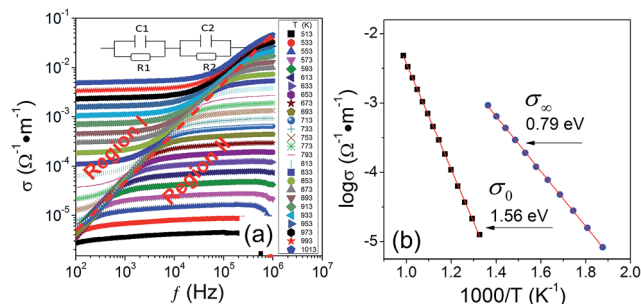
Fig. 7 (a) The frequency dependence of AC conductivity of BZO measured at different temperatures. (b) The Arrhenius plots of the conductivity with the data deduced from regions I and II as shown in (a).

serially connected RC (R = resistor and C = capacitor) units with the subindex 1 and 2 referring to the bulk and interfacial effects, respectively. Based on the equivalent circuit, the AC conductivity can be written as:[39]

$$\sigma(\omega) = \sigma_\infty + \frac{\sigma_0 - \sigma_\infty}{1 + (\omega\tau)^2} \tag{3}$$

where $\omega = 2\pi f$ is angular frequency, τ is relaxation time, σ_0 and σ_∞ are the conductivity at $\omega = 0$ and ∞, respectively. Eqn (3) is formally equivalent to the well-known Debye relaxation equation. Clearly, the AC conductivity shows a low-frequency plateau (σ_0) and a high-frequency plateau (σ_∞) with a sigmoidal curve linking them. It was reported that the low- and high-frequency plateaus, i.e., regions I and II in Fig. 7(a), correspond to the interfacial and bulk contributions, respectively.[39] The Arrhenius plots of σ_0 and σ_∞ deduced from regions I and II, respectively, were plotted in Fig. 7(b). The activation energy for σ_0 and σ_∞ was calculated to be 0.79 and 1.56 eV, respectively. These values agree well with the corresponding activation energy values for $R1$ and $R2$. This finding further demonstrates that $R1$ and $R2$ are bulk and interfacial responses, respectively.

Finally, it is worthwhile to compare the dielectric properties between pure and acceptor-doped BZO ceramics. The relaxing species in pure BZO are the inherent defects of oxygen vacancies. The observed dielectric relaxations are associated with the migration of the vacancies. Whereas the acceptor-doped BZO ceramics become the well-known proton conducting oxides.[40] There are two distinctly important types of carriers: hydroxyl ions ($OH_O^\cdot$) and oxygen vacancies ($V_O^{\cdot\cdot}$) in the samples. These carriers may associated with the dopants, such as Y or Zr, giving rise to complex dipole pairs ($OH_O^\cdot - Y$, $OH_O^\cdot - Zr$, $V_O^{\cdot\cdot} - Y$ and $V_O^{\cdot\cdot} - Y$). The high-temperature dielectric properties are thereby determined by the complex dipoles.[40,41] Besides, the grain boundaries instead of the sample/electrode contacts in the acceptor-doped BZO have been widely evidenced to show higher resistance than the interior of the grains and hinder the migration of charged carriers.[42–44]

4. Conclusions

In summary, BZO powders were synthesized by solution combustion based on the glycine nitrate process. The sample sintered at 1973 K for 12 h was found to show optimal dielectric properties. It was found that BZO showed incipient ferroelectric behavior in the temperature range below 420 K. Above this temperature, CDC behavior appears composed of two sets of oxygen-vacancy-related relaxations ($R1$ and $R2$). The low-temperature relaxation $R1$ was attributed to be a dipolar relaxation due to hopping oxygen vacancies inside grains, while the high-temperature relaxation $R2$ was argued to be a Maxwell–Wagner-type relaxation related to the vacancies blocked by the sample/electrode contacts.

References

1 M. Viviani, M. Bassoli, V. Buscaglia, M. T. Buscaglia and P. Nanni, *J. Phys. D: Appl. Phys.*, 2009, **42**, 175407.
2 M. E. Mchenry and D. E. Laughlin, *Acta Mater.*, 2000, **48**, 223–238.
3 G. A. Govor and V. V. Mikhnevich, *Inorg. Mater.*, 2007, **43**, 711–713.
4 S. Guillemet-Fritsch, Z. Valdez-Nava, C. Tenailleau, T. Lebey, B. Durand and J.-Y. Chane-Ching, *Adv. Mater.*, 2008, **10**, 551–555.
5 M. A. Subramanian, D. Li, N. Duan, B. A. Reisner and A. W. Sleight, *J. Solid State Chem.*, 2000, **151**, 323–325.
6 N. Lei and X. M. Chen, *Appl. Phys. Lett.*, 2007, **91**, 122905.
7 A. P. Ramirez, M. A. Subramanian, M. Gardel, G. Blumberg, D. Li, T. Vogt and S. M. Shapiro, *Solid State Commun.*, 2000, **115**, 217–220.
8 G. J. Wang, C. C. Wang, S. G. Huang, C. M. Lei, X. H. Sun, T. Li and L. N. Liu, *J. Am. Ceram. Soc.*, 2013, **96**, 2203–2210.
9 X. H. Sun, C. C. Wang, G. J. Wang, C. M. Lei, T. Li and L. N. Liu, *J. Am. Ceram. Soc.*, 2013, **96**, 513–518.
10 W. Xia, C. C. Wang, P. Liu, J. L. Ye and W. Ni, *Curr. Appl. Phys.*, 2013, **13**, 1743–1745.
11 J. Zhang, Y. Li, D. Zhang, H. C. Qi, X. X. Xu, Z. F. Huang and C. C. Wang, *Mater. Lett.*, 2016, **168**, 163–165.
12 Y. M. Guo, Y. Lin, R. Ran and Z. P. Shao, *J. Power Sources*, 2009, **193**, 400–407.
13 L. Malavasi, C. A. J. Fisher and M. S. Islam, *Chem. Soc. Rev.*, 2010, **39**, 4370–4387.
14 Y. Yamazaki, R. Hernandez-Sanche and S. M. Haile, *Chem. Mater.*, 2009, **21**, 2755–2762.
15 F. Iguchi, N. Sata, T. Tsurui and H. Yugami, *Solid State Ionics*, 2007, **178**, 691–695.
16 M. Arrigoni, T. S. Bjørheim, E. Kotomin and J. Maier, *Phys. Chem. Chem. Phys.*, 2016, **18**, 9902–9908.

17 T. S. Bjørheim, M. Arrigoni, S. W. Saeed, E. Kotomin and J. Maier, *Chem. Mater.*, 2016, **28**, 1363–1368.

18 A. R. Akbarzadeh, I. Kornev, C. Malibert, L. Bellaiche and J. M. Kiat, *Phys. Rev. B: Condens. Matter Mater. Phys.*, 2005, **72**, 205104.

19 T. Maiti, R. Guo and A. S Bhalla, *J. Appl. Phys.*, 2006, **100**, 114109.

20 T. Maiti, E. Alberta, R. Guo and A. S. Bhalla, *Mater. Lett.*, 2006, **60**, 3861–3865.

21 X. G. Tang, K. H. Chew and H. L. W. Chan, *Acta Mater.*, 2004, **52**, 5177–5183.

22 H. Stetson and B. Schwartz, *J. Am. Ceram. Soc.*, 1961, **44**, 420–421.

23 R. Viana, P. Lunkenheimer, J. Hemberger, R. Böhmer and A. Loidl, *Phys. Rev. B: Condens. Matter Mater. Phys.*, 1994, **50**, 601–604.

24 W. Zhong and D. Vanderbilt, *Phys. Rev. B: Condens. Matter Mater. Phys.*, 1996, **53**, 5047–5050.

25 A. R. Akbarzadeh, L. Bellaiche, K. Leung, J. Iñiguez and D. Vanderbilt, *Phys. Rev. B: Condens. Matter Mater. Phys.*, 2004, **70**, 054103.

26 J. H. Barrett, *Phys. Rev.*, 1952, **86**, 118–120.

27 J. F. Scott, *Ferroelectric memories*, Springer, Berlin, 2000.

28 C. C. Wang, J. Wang, X. H. Sun, L. N. Liu, J. Zhang, J. Zheng and C. Cheng, *Solid State Commun.*, 2014, **179**, 29–33.

29 H. S. Shulman, D. Damjanovic and N. Setter, *J. Am. Ceram. Soc.*, 2000, **83**, 528–532.

30 C. Ang, Z. Yu and L. E. Cross, *Phys. Rev. B: Condens. Matter Mater. Phys.*, 2000, **62**, 228–236.

31 C. C. Wang, C. M. Lei, G. J. Wang, X. H. Xun, T. Li, S. G. Huang, H. Wang and Y. D. Li, *J. Appl. Phys.*, 2013, **113**, 094103.

32 C. M. Lei, C. C. Wang, G. J. Wang, X. H. Sun, T. Li and L. Liu, *J. Alloys Compd.*, 2013, **555**, 51–55.

33 M. Kuwabara, K. Goda and K. Oshima, *Phys. Rev. B: Condens. Matter Mater. Phys.*, 1990, **42**, 10012.

34 S. Steinsvik, R. Bugge, J. Gjonnes, J. Tafto and T. Norby, *J. Phys. Chem. Solids*, 1997, **58**, 969–976.

35 C. C. Wang, M. N. Zhang, K. B. Xu and G. J. Wang, *J. Appl. Phys.*, 2012, **112**, 034109.

36 C. C. Wang, M. He, F. Yang, J. Wen, G. Z. Liu and H. B. Lu, *Appl. Phys. Lett.*, 2007, **90**, 192904.

37 H. B. Li, Q. J. Li, J. Zhang, S. G. Huang, Y. Yu, J. Zheng, C. Cheng and C. C. Wang, *J. Eur. Ceram. Soc.*, 2016, **36**, 2513–2518.

38 A. K. Jonscher, *Nature*, 1977, **267**, 673–679.

39 M. Zhu, N. Zhang, H. Wang, Y. D. Li, S. G. Huang, Q. J. Li, Y. Yu, Y. M. Guo, X. L. Liu and C. C. Wang, *RSC Adv.*, 2017, **7**, 26130–26135.

40 K. D. Kreuer, *Annu. Rev. Mater. Res.*, 2003, **33**, 333–359.

41 O. Kamishima, Y. Abe, T. Ishii, J. Kawamura and T. Hattori, *J. Phys.: Condens. Matter*, 2004, **16**, 4971–4981.

42 F. Iguchi, C.-T. Chen, H. Yugami and S. Kim, *J. Mater. Chem.*, 2011, **21**, 16517–16523.

43 M. Shipour, R. Merkle and J. Maier, *Solid State Ionics*, 2012, **225**, 304–307.

44 M. Shipour, R. Merkle and J. Maier, *Solid State Ionics*, 2012, **216**, 1–5.